Discrete-element model for dynamic fracture of a single particle

Luisa Fernanda Orozco, Jean-Yves Delenne, Philippe Sornay, Farhang Radjai

Discrete-element model for dynamic fracture of a single particle

Luisa Fernanda Orozco[a,b], Jean-Yves Delenne[c], Philippe Sornay[a], Farhang Radjai[b,*]

[a] CEA, DEN, DEC, SA3E, LCU, Saint Paul les Durance 13108, France
[b] LMGC, CNRS, University of Montpellier, France
[c] IATE, INRA, CIRAD, Montpellier SupAgro, University of Montpellier, France

A B S T R A C T

We investigate the dynamic fracture of a single particle impacting a flat surface using 3D DEM simula- tions based on a fragmentation model involving both a stress threshold and a fracture energy. The particle is assumed to be perfectly rigid and discretized into polyhedral Voronoï cells with cohesive interfaces. A cell-cell interface loses its cohesion when it is at a normal or tangential stress threshold and an amount of work equal to the fracture energy is absorbed as a result of the relative cell-cell displacements. Upon impact, the kinetic energy of the particle is partially consumed to fracture cell-cell contacts but also restituted to the fragments or dissipated by inelastic collisions. We analyze the damage and fragmenta- tion efficiency as a function of the impact energy and stress thresholds and their scaling with fracture energy and impact force. In particular, we find that the fragmentation efficiency, defined as the ratio of the consumed fracture energy to the impact energy, is unmonotonic as a function of the impact energy, the highest efficiency occurring for a specific value of the impact energy.

Keywords:
Granular materials
DEM
Contact dynamics
Impact test
Fracture energy
Damage

1. Introduction

Particle breakage takes place in numerous natural and industrial processes, and it has been addressed in multiple research fields and applications such as powder technology, construction engineering, mining, food industry and metallurgy (Tarasiewicz and Radziszewski, 1990; Vogel and Peukert, 2003; Leite et al., 2011; Xu et al., 2017). The processes that involve particle breakage range from rock fracture in landslide events to the grinding of minerals in various applications (Varnes, 1958; Touil et al., 2006; Bailon-Poujol et al., 2011). The initiation and evolution of particle fragmentation are governed by fracture mechanics at the material level and by granular dynamics at the particle packing scale. For this reason, it is necessary to enhance our understanding of the effects of various parameters that control fracture-induced phenomena independently of the specific crushing or grinding machines employed in different applications. For example, it is well known that the comminution is an energy-intensive transformation and the size distribution of reduced particles is crucially dependent on various factors related to the material and loading conditions (Tavares and King, 1998; Fuerstenau and Abouzeid, 2002; Stamboliadis, 2007; Govender, 2016; Mayer-Laigle et al., 2018). But most of the present knowledge on the energy consumption and its dependence on the material properties is empirical in nature. Different loading modes such as compression, distortion, shear, and impact can cause particle fracture, and their combination leads to a multitude of local mechanisms such as damage and abrasion that take place simultaneously during a comminution process (Tarasiewicz and Radziszewski, 1990; Govender, 2016; Kim and Santamarina, 2016).

Studying the fracture of a single particle is the first step towards a quantitative description of the complex multi-particle fracture dynamics. Experimentally, the previous work on the fragmentation of one particle has been largely focused on compression tests under quasi-static conditions (Chau et al., 2000; Brzesowsky et al., 2011). Dynamic fracture tests have been performed by means of drop weight impact (Tavares and King, 1998; Wu et al., 2004; Ge et al., 2017) or air gun (Salman et al., 2002). Large-scale experiments were also performed on the fragmentation of rocks falling on a hard surface (Giacomini et al., 2009). The common goal of single-particle tests has been to investigate the fragment size distribution, crack patterns, particle breakage probability, and failure modes (Potapov and Campbell, 1994; Kun and Herrmann, 1998; Tsoungui et al., 1999; Subero et al., 1999; Chau et al., 2000; Salman et al., 2002; Wittel et al., 2008; Casini et al., 2013; Huang et al., 2014). Several authors have also considered the fracture energy consumed per unit mass (Stamboliadis, 2007; Tavares and King, 1998; Fuerstenau and Abouzeid, 2002; Casini et al., 2013). This is the energy consumed in producing new fractured surfaces inside the particle. Other sources of energy dissipation in the

* Corresponding author.
E-mail address: franck.radjai@umontpellier.fr (F. Radjai).

fragmentation process are the plastic deformations and frictional or inelastic collisions. Part of the total impact energy is also taken away by the kinetic energy of the fragments, for which we found no reported measurements in the available literature. Most measurements were carried out at the end of the tests because of the difficulty of measuring in real time the stress distributions and particle motions (Wittel et al., 2008).

On the numerical modeling side, the simulation of particle fragmentation began with Finite Element Method (FEM) approaches wherein the dynamic meshes make it possible to incorporate cracks and their evolution in time (Hillerborg et al., 1976; Zubelewicz and Bažant, 1987). Later, the discrete element method (DEM) was used as the privileged tool for the simulation of granular materials with the advantage of incorporating various particle interactions such as friction, cohesion and damage, and providing access to the forces and velocities at the particle scale (Cundall and Strack, 1979; Moreau and Solids, 1994; Radjai and Richefeu, 2009; Delenne et al., 2004; Taboada et al., 2006; Luding, 2008; Herrmann and Luding, 1998). Within the framework of the DEM, particle fragmentation has often been modeled using the Bonded Particle Method (BPM), in which the particles are modelled as agglomerates of glued disks (Thornton et al., 1996) or spheres (Subero et al., 1999; Mishra and Thornton, 2001; McDowell and Harireche, 2002; Moreno-Atanasio and Ghadiri, 2006). An issue with this method is that the total volume of the material is not conserved during the fragmentation process. Another method consists in replacing parent particles by smaller ones once a local failure criterion is achieved. It has been applied to packings of disks (Tsoungui et al., 1999; Lobo-Guerrero et al., 2006), spheres (Ciantia et al., 2015; Bruchmüller et al., 2011) and polyhedral particles (Eliáš, 2014). A variant of the first method consists in replacing spherical primary particles by multiple polygonal cells in 2D (Potapov and Campbell, 1994; Kun and Herrmann, 1996; Nguyen et al., 2015) or polyhedral cells in 3D (Galindo-Torres et al., 2012; Cantor et al., 2017), a method that was coined Bonded Cell Method (BCM).

In most discrete models of particle fracture using the BPM, the cohesive behavior at the inter-cell contacts is of brittle type and governed by a force or stress threshold. A pre-failure plastic force model was proposed by Luding (2008) by introducing two independent stiffness parameters for loading and unloading force-displacement relations, respectively. This plastic contact model, however, concerns only the normal compressive part of the displacement, the failure in tension being simply governed by a force threshold. Another plastic contact model was proposed by Timár et al. (2010) who introduced a healing time so that whenever two particles remain in contact for a time longer than this time, a new cohesive link is inserted between them. This process gradually modifies the reference elastic configuration of the particles and leads to plastic dissipation and permanent deformation. The power-law distribution of fragment masses found by using this approach was found to be in good agreement with fracture experiments performed with polymeric particles.

In this paper, we introduce a fracture law within a discrete element approach that involves both a stress threshold and a fracture energy in normal and tangential directions. This model is implemented at the inter-cell interfaces inside the particle in a three-dimensional BCM approach. The introduction of an energy criterion allows for the simulation of dynamic fracture in impact tests. A cell-cell interface breaks only if the stress threshold is reached and the work absorbed by the interface due to relative displacements along the normal and tangential directions is above the fracture energy. Using this method, we investigate the breakage of a single particle impacting a rigid plane by means of extensive simulations. We analyze the total fracture energy, i.e. the energy consumed due to debonding of cell-cell contacts, as a function of the impact velocity. In particular, we show that the fragmentation efficiency, defined as the ratio of the total fracture energy to the impact energy has a maximum value for a specific value of the impact energy. We introduce a fitting form that captures the observed behavior over the whole range of investigated energies. We also consider the effects of the normal strength as well as the ratio of normal to tangential thresholds.

In the following, we first introduce in Section 2 the numerical approach, with focus on the fracture model, and general conditions of the impact test. Then, in Section 3, we analyze particle damage and fragmentation efficiency as a function of the impact velocity and fracture energy. In Section 4, we consider the effective restitution coefficient and energy dissipation by impact. In Section 5, we focus on the effect of the stress thresholds and friction coefficient. Finally, in Section 6, we briefly present the salient results of this work and its possible extensions.

2. Numerical method and procedures

In this section, we present different ingredients of our numerical approach for the simulation of particle fragmentation under impact. We use the Bonded Cell Method (BCM) based on the division of the particle into polyhedral cells interacting with their neighboring cells via an interface characterized by a debonding stress threshold and a fracture energy (Nguyen et al., 2015; Cantor et al., 2017). We describe the interface behavior, followed by the tessellation method and our DEM algorithm for dynamic simulation of the particle.

2.1. Bonded-cell method

In BCM, the polyhedral cells of a particle interact only through their interface areas and they are assumed to behave as independent rigid particles so that their dynamic behavior can be simulated by the DEM. During the fragmentation process, a subset of cell-cell interfaces break and the parent particle gives rise to fragments, each composed of several bonded cells. We used the Voronoï tessellation method for the division of the particle into random cells by means of the software NEPER (Quey et al., 2011). The cells are always convex and present adjacent faces. For the sake of geometrical consistency between a particle and its constitutive polyhedral cells, we use particles of icosahedral shape in the simulations. The number of Voronoï mesh elements determines the maximum number of potential fragments that can be generated as a result of the fragmentation of a particle. Cantor et al. and Nguyen et al. used the BCM for quasi-static diametrical compression of particles (Nguyen et al., 2015; Cantor et al., 2017). They found that the particle strength depends on the ordering of the cellular structure of particles. For this reason, we generate fully random cells both in their sizes and shapes. Fig. 1 displays several examples of particles with increasing numbers of cells.

The cell-meshed particles in BCM are similar to aggregates of primary particles or particulate compounds in the Bonded Particle Method (BPM). There are, however, fundamental differences between a particulate compound and a particle in BCM. In the first place, a particle in BCM has zero porosity, so that the total volume of the particle is conserved during its fracture whereas the total volume of a particulate compound of spherical particles of nearly the same size is reduced by 40% when fully broken into its primary particles. Furthermore, the interfaces between cells in BCM are well-defined surface areas whereas in BPM they are pointwise contacts between primary spherical particles. Hence, the debonding stress threshold of the cell-cell interfaces can be directly set equal to the tensile strength of the particle and the debonding force is given by tensile strength multiplied by the cell-cell interface area.

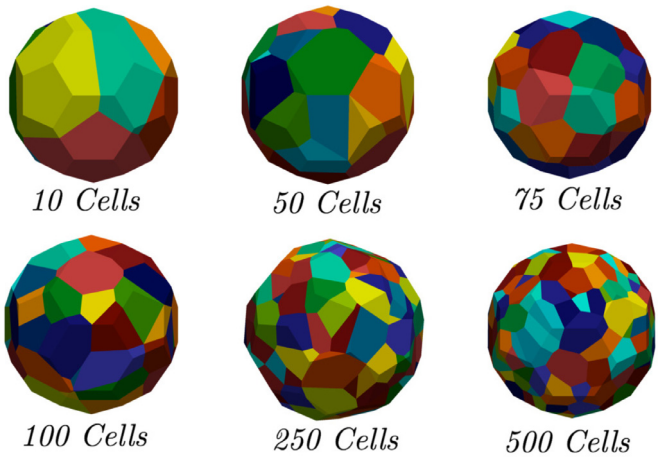

Fig. 1. Particles generated with different numbers of cells which are represented by different colors.

2.2. Internal cohesion and fracture

In BCM, the cells should interact through an interface mechanical behavior pertaining to the nature of the material. In its most general form, this interface behavior is characterized by a relationship between the normal and tangential components of the cell-cell stress, on one hand, and the relative cell displacement or velocity, on the other hand. We also need a criterion for debonding, i.e. the loss of internal cohesion and thus creation of a cohesionless frictional interface between two cells.

In most discrete-element models applied to particulate compounds, the material parameters are the elastic moduli, and debonding is governed by a normal and/or tangential force threshold. Hence, in these models the creation of cohesionless surface and its propagation do not explicitly obey the thermodynamic Griffith criterion in which the propagation of a crack requires that an amount of work per unit area equal to or larger than the fracture energy G_f to be supplied by the action of external forces or from the variation of the elastic energy (Hillerborg et al., 1976; Rice, 1978). The original Griffith formulation is based on a differential criterion, assuming that the crack growth is continuous. Hence, it can not be applied as such to a cell-cell interface in BCM, which in the sprit of DEM must fail as a whole by releasing a finite area s. In other words, it is not desirable and computationally efficient to consider sub-cell scales and the time process of crack propagation inside the interface. For this reason, an incremental form of the energy criterion should be applied (Leguillon, 2002):

$$-\frac{\Delta W_p}{s} \geq G_f, \tag{1}$$

where ΔW_p is the variation of the potential energy.

In order to use Eq. (1) in DEM, we also need to express the variation ΔW_p of the potential energy in terms of cell displacements as the cells are considered to be rigid so that all interface variables reflect those of cells. We also need to separate tensile and shear components u_n and u_t, respectively, of the relative displacement of the cells at the interface. For an interface at tensile or shear stress threshold, the work G_n or G_t performed by the stress from the time when the stress threshold is reached t_0 to the time t is given by

$$G_n(t) = \int_{t_0}^{t} C_n u_n \, dt = C_n \Delta_n(t), \tag{2}$$

$$G_t(t) = \int_{t_0}^{t} C_t u_t \, dt = C_t \Delta_t(t), \tag{3}$$

where C_n and C_t are the tensile and shear stress thresholds, respectively. Either G_n or G_t (depending on whether the normal stress or the shear stress is at its threshold), is the work absorbed by the interface, and assuming that ΔW_p is fully consumed in this work, according to (1) the interface fails at time t_1 when either

$$G_n(t_1) = G_{fn} = C_n \ell_n, \tag{4}$$

or

$$G_t(t_1) = G_{ft} = C_t \ell_t, \tag{5}$$

where G_{fn} and G_{ft} are fracture energies for normal and tangential rupture, respectively, $\ell_n = \Delta_n(t_1)$ and $\ell_t = \Delta_t(t_1)$. In this way, a cell-cell interface fails when the stress threshold is reached and the cumulative work absorbed by the interface due to the relative displacements along the normal or tangential direction is equal to the corresponding fracture energy.

Note that the formulation of the energy criterion in terms of finite increments is consistent with the Finite Fracture Mechanics based on the assumption that crack propagation always occurs over a minimal length $\ell_n \approx G_{fn}/C_n$ or $\ell_t \approx G_{ft}/C_t$ (Leguillon, 2002). A similar length scale is also introduced in Cohesive Zone models in which it is assumed that the material is micro-cracked and can still transmit stresses in a region of finite length behind the crack tip (Hillerborg et al., 1976). In our formulation of the work calculated from cell displacements in equations (2) and (3), the length scales ℓ_n and ℓ_t represent the orders of magnitude of the relative normal and tangential displacements before failure. Hence, the ratios ℓ_n/d_c and ℓ_t/d_c, where d_c is the mean cell diameter, are the inelastic deformations of a particle before fragmentation. As large inelastic deformations must be avoided in DEM simulations (as we want the cells to keep their close neighbors as long as the fracture has not occurred), it is important to make sure that the cell size d_c is large compared to the ratios G_{fn}/C_n and G_{ft}/C_t.

In practice, when a stress threshold is reached at an interface, the two connected cells are allowed to separate or slide along their interface. But, even if the corresponding relative cell velocities u_n and u_t are different from 0, the interface is allowed to carry a normal force sC_n or a tangential force sC_t. In other words, the interface remains active and stress-transmitting although the two cells can move with respect to each other. Let f_n and f_t be the normal and tangential interface forces, respectively, and μ the coefficient of friction. For the implementation, our interface model can be expressed by the following relations:

$$\begin{cases} G_n \leq G_{fn} & \wedge \begin{cases} \Delta_n = 0 & \Rightarrow \quad f_n \geq -C_n s \\ \Delta_n > 0 & \Rightarrow \quad f_n = -C_n s \end{cases} \\ G_n > G_{fn} & \wedge \begin{cases} \Delta_n = 0 & \Rightarrow \quad f_n \geq 0 \\ \Delta_n > 0 & \Rightarrow \quad f_n = 0 \end{cases} \end{cases} \tag{6}$$

$$\begin{cases} G_t \leq G_{ft} & \wedge \begin{cases} \Delta_t > 0 & \Rightarrow \quad f_t = -C_t s \\ \Delta_t = 0 & \Rightarrow \quad -C_t s \leq f_t \leq C_t s \\ \Delta_t < 0 & \Rightarrow \quad f_t = C_t s \end{cases} \\ G_t > G_{ft} & \wedge \begin{cases} \Delta_t > 0 & \Rightarrow \quad f_t = -\mu f_n \\ \Delta_t = 0 & \Rightarrow \quad -\mu f_n \leq f_t \leq \mu f_n \\ \Delta_t < 0 & \Rightarrow \quad f_t = \mu f_n \end{cases} \end{cases} \tag{7}$$

Fig. 2 shows a graphical representation of these relations. Note that, the interface becomes noncohesive only in the cases where $f_n = 0$ or $|f_t| = \mu f_n$.

Once an interface loses its cohesion, it turns into a purely frictional contact. If the gap created as a result of interface deformation is nonzero ($\Delta_n > 0$), the normal and tangential forces are both zero and the created contact is open. Otherwise ($\Delta_n = 0$), the contact remains active and the relation between the normal force f_n and the relative normal velocity u_n is governed by the Signorini

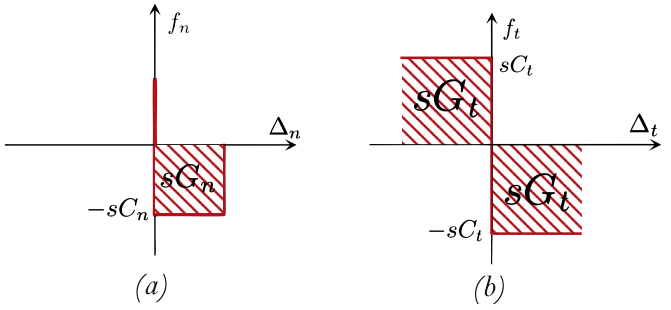

Fig. 2. Interface behavior along (a) normal direction and (b) tangential direction. The solution for each pair (Δ_n, f_n) and (Δ_t, f_t) lies on the thick line. See the text for the definition of the variables.

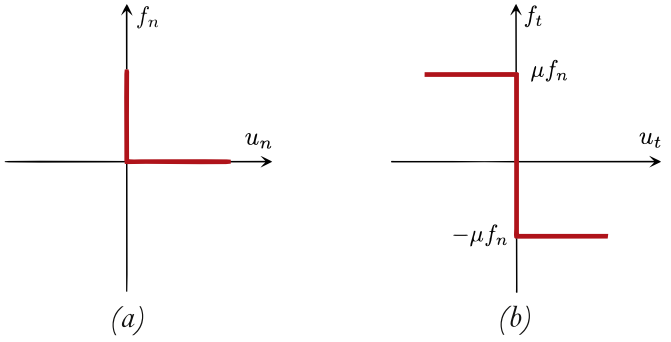

Fig. 3. Frictional contact law defined at the contact framework in the (a) normal direction (b) tangential direction.

inequalities:

$$\begin{cases} \Delta_n = 0 & \wedge & \begin{cases} u_n = 0 & \Rightarrow & f_n \geq 0 \\ u_n > 0 & \Rightarrow & f_n = 0 \end{cases} \\ \Delta_n > 0 & \Rightarrow & f_n = 0 \end{cases} \tag{8}$$

These inequalities are shown in Fig. 3 as a graph (Jean et al., 2001). In the same way, the frictional component is governed by the Coulomb dry friction inequalities between the friction force f_t and the relative tangential velocity u_t:

$$\begin{cases} \Delta_n = 0 & \wedge & \begin{cases} u_t > 0 & \Rightarrow & f_t = -\mu f_n \\ u_t = 0 & \Rightarrow & -\mu f_n \leq f_t \leq \mu f_n \\ u_t < 0 & \Rightarrow & f_t = \mu f_n \end{cases} \\ \Delta_n > 0 & \Rightarrow & f_t = 0 \end{cases} \tag{9}$$

shown in Fig. 3(b). The rigid-plastic contact model introduced in this work is similar in spirit to that introduced by Timár et al. (2010) in which the elastic beams connecting the particles are re-established after a healing time, allowing thus for plastic (irreversible) deformation. In our model, the particle does not break as long as the work is below the fracture energy. This means that the particle can deform as a whole without failure.

2.3. Contact dynamics

For the simulation of the dynamics of undeformable particles (including rigid cells in this work), we employed the Contact Dynamics (CD) method (Moreau, 1993; Jean et al., 2001; Radjai and Richefeu, 2009). As in molecular dynamics (MD) or similar DEM algorithms, the equations of motion are integrated in time by means of a time-stepping scheme. However, in contrast to MD, the Signorini and Coulomb inequalities are implemented in CD as constraints that are taken into account for the calculation of contact forces and velocities in an implicit scheme. An iterative algorithm is used to calculate simultaneously at all contacts and interfaces the relative velocities and forces at the end of each time step. It should be noted that, as in the CD method the interface and contact behaviors are not based on an elastic force law involving the overlap between particles (or cells), the time step can be large, and the calculated force represents a time-averaged force during a time step.

The implicit nature of the CD method can be described as follows:

1. A network of potential contacts (or interfaces) is defined from the particle positions.
2. The contact forces and velocities are calculated by an iterative process accounting for equations of motion together with the Coulomb and Signorini relations.
3. The particle positions and rotations are updated.

The second step ensures that, when the particles are moved according to their computed velocities, they will not overlap at the end of the time step. Because of this implicit nature of the method, the time-stepping scheme is unconditionally stable, so that large time steps can be used.

It is also important to mention here the meaning of the restitution coefficient in the framework of the CD method. For a collision between two particles, the normal and tangential restitution coefficients, e_n and e_t respectively, are classically defined from the relative normal and tangential velocities after and before the collision. This concept can not be used in a dense granular material in which the particle momentum involves a network of particles so that the momenta propagate through the whole contact network and may leave the system through the boundary conditions. In the CD method, a conceptually different approach is used. In fact, the Signorini and Coulomb relations (8) and (9) involve the velocities u_n and u_t, which represent the relative velocities at the end of a time step because of the implicit formulation of the time-stepping scheme. But a more general approach consists in replacing these velocities by weighted means (Moreau, 1993; Radjai and Richefeu, 2009):

$$u_n = \frac{u_n^+ + e_n u_n^-}{1 + e_n}, \tag{10}$$

$$u_t = \frac{u_t^+ + e_t u_t^-}{1 + |e_t|}, \tag{11}$$

where u_n^- and u_t^- are the velocities at the beginning of the time step and u_n^+ and u_t^+ are the velocities at the end of the time step. According to (10), a contact occurs between two particles when $u_n = 0$, implying $u_n^+ = -e_n u_n^-$, which corresponds to the common interpretation of e_n. But, in contrast to this classical definition of e_n, the condition $u_n^- = 0$ (i.e. a persistent contact) does not necessarily lead to $u_n^+ = 0$. The latter can only arise as a solution of global determination of forces and velocities through an iterative process together with relation (10) in which $u_n^- = 0$. For the tangential restitution coefficient, the condition $u_t^- = 0$ means that a contact is in the rolling state (no sliding but one particle rolling on the other or simply no relative motion). The above discussion regarding the normal velocities applies also to the tangential velocities.

For the interface between cells, as long as the cohesion is effective, the relative velocity of the cells should be interpreted as inelastic deformations localized inside the interface. This means that the coefficient of restitution should be consistently set to zero. This is also true for cohesionless contacts between cells since their configuration inside the particle is too dense (with zero porosity) for a normal restitution coefficient to be effective. For these reasons, in all simulation results reported in this paper we set $e_n = e_t = 0$.

In application to cells of polyhedral shape, the CD method should resolve also the types of contacts between the cells at

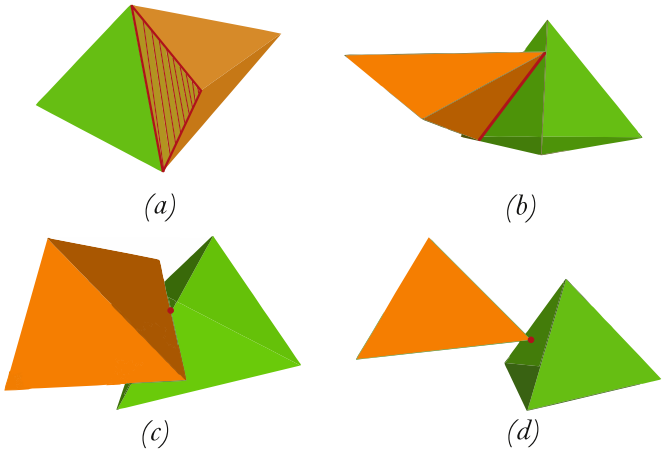

Fig. 4. Generic contact types between polyhedra.

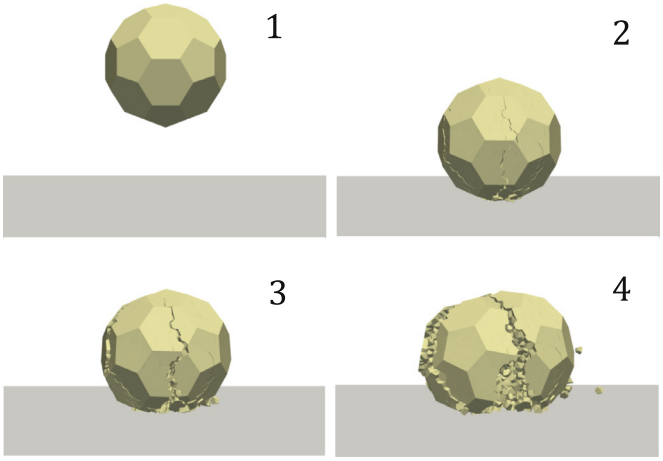

Fig. 5. Snapshots of a particle impacting a rigid plane, and the evolution of particle breakage. This test was performed with an impact velocity of 6 m/s.

each time step before the iterative determination of dynamic variables. There can be several types of contacts between two polyhedra: face-face, face-edge, edge-edge, vertex-face,.... Geometrically, a face-face contact is a plane and it can be represented by three points (termed 'triple contact'). A face-edge contact is a line and can be characterized by two points (termed 'double contact'); see Fig. 4. A vertex-face contact is a point termed 'single contact'. The edge-edge contacts are generally of single type whereas vertex-vertex and parallel edge-edge contacts are statistically rare and their occurrence sensitively depends on the geometrical precision of the detection procedure. To determine the contact types, we use the Cundall Common Plan method (Cundall, 1988) and we attribute three points to a triple contact, two points to a double contact and one point to a single contact. All points are treated as independent point contacts to which the iterative procedure described previously is applied. The contact force of a triple or double contact is the resultant force of the three or two forces acting at the corresponding points with its application point determined as their centroid.

The initial Voronoï tessellation of a particle leads to a configuration of polyhedral cells that, by construction, have face-face, vertex-vertex and parallel edge-edge contacts. We only consider the face-face contacts that define the cohesive interfaces. The edge-edge and vertex-vertex contacts in the cell configuration are omitted as the internal cohesion of the particle is carried by the interfaces. However, as the cells move or fracture at their interfaces, contacts of other types may occur, and the consequent evolution needs to detect periodically the contacts. Because of its treatment of contacts as geometrical constraints, the CD method provides in this way a general framework for the simulation of particles of arbitrary shape. For the simulations, we used the CD method as implemented in the software LMGC90 (Dubois et al., 2011).

2.4. Impact test

To investigate the fragmentation of particles, we perform impact tests, which consist in releasing a particle from a height equal to 2 times its radius, measured from the lowest point of the particle, onto a rigid plane. In order to study the effect of the impact energy W_k^- (kinetic energy of the particle before collision), the impact velocity was varied by applying an initial velocity to the particle with the gravity set to $g = 9.81$ m/s^2. The impact energy is given by $W_k^- = mv^2/2$, where v is the particle velocity at impact time with the plane and m is the particle mass. We used a particle diameter equal to 1 mm in all tests. The friction coefficient between the particle and the plane was set to 0.4. Each impact test was repeated 10 times, each with a different tessellation of the particle into cells. The data points presented in the following are average values over the 10 tests with an error bar representing their standard deviation. It should also be noted that the point of impact with the plane is random, so that the particle, which has a polyhedral external shape, can fall on a face, edge or vertex. To avoid systematic errors due to this effect, we rotate the particle in an arbitrary direction before each impact test. A sequence of snapshots of a particle during an impact test is shown in Fig. 5.

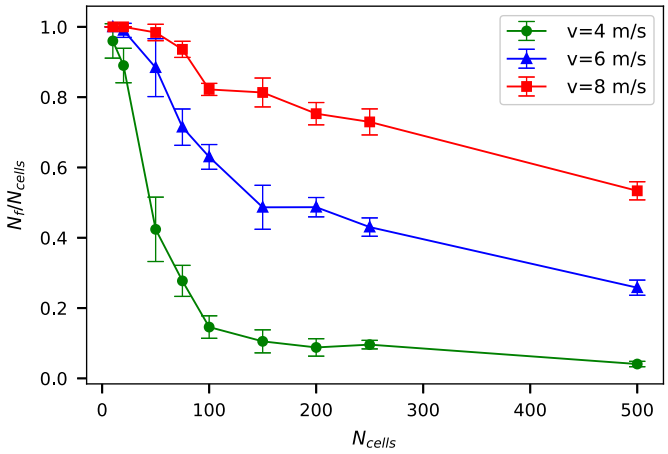

Fig. 6. Effect of the number of cells on the number of generated fragments for three different values of the impact velocity.

In all the simulations described in this paper, we set $G_{fn} = G_{ft} \equiv G_f$ with several values in the range [0.2,2] J/m^2, corresponding to typical measured values of the fracture energy for glass beads. We performed a parametric study by changing the impact velocity up to 10 m/s, the interface stress thresholds C_n and C_t up to 15 MPa, and the friction coefficient μ between fragments from 0.2 to 0.6.

The objectivity of a fracture model requires the fracture process to be independent of numerical parameters. In our BCM model, the numerical parameters are related to the Voronoï tessellation and the number of cells N_{cells}. For the tessellation, we use the most random distribution of cells but their number may influence the fracture process. Fig. 6 shows the number of fragments N_f as a function of N_{cells} for three different values of the impact velocity. We see that the number of fragments declines as N_{cells} increases, but asymptotically tends to a constant value independent of N_{cells}. Typically, we need at least 100 cells in each particle in order to

reduce the finite size effects that influence the number of fragments for lower numbers of cells. For this reason, in all simulations of impact test we used 100 cells to tessellate the particles. We analyze in detail below the effects of various parameters on the particle fracture.

3. Damage and fragmentation efficiency

During an impact, part of the initial kinetic energy W_k^- of the particle is transmitted to the fragments. Let W_k^+ be the total energy of the fragments. The difference $W_d = W_k^- - W_k^+$ is consumed in fracture and possibly dissipative interactions, including friction and inelastic collisions, between fragments. If s is the total cohesionless surface area created during fracture, the total fracture energy is given by

$$W_f = sG_f. \tag{12}$$

In the framework of the BCM, this energy may be compared with the total fracture energy $W_f^T = s^T G_f$ required to break all cell-cell interfaces of total area s^T. Hence, the particle damage can be defined as

$$D_w = \frac{W_f}{W_f^T} = \frac{s}{s^T}. \tag{13}$$

Obviously, the value of s^T depends on the size or number of cells. The physical meaning of this limit in materials can be related to the scale of heterogeneities. For example, in a porous material of porosity ϕ with a distribution of pores of typical volume V_p, the mean-free path $\ell = (V_p/\phi)^{1/3}$ may be considered as the typical size of elementary cells (Laubie et al., 2017). In such materials, as a result of stress concentration, the value of fracture energy is far below the theoretical threshold of the same material without pores. For this reason, the fracture energy of fragments of size ℓ is much higher than the initial porous samples. In the same way, in materials with a granular texture, the grains are usually much harder than their assembly, and thus the grains play the role of building blocks as the cells in our model material.

A crucial aspect of comminution is its energetic efficiency, i.e. the amount of energy consumed for fracture as a function of impact energy. We define the fragmentation efficiency η as the ratio of the total fracture energy to the impact energy:

$$\eta = \frac{W_f}{W_k^-}. \tag{14}$$

The comminution is generally not an efficient process in the sense that most of the supplied energy is not consumed in fracture. It is thus interesting to see how the value of η for a single particle depends on the impact parameters. This information can then be used to understand and predict the fragmentation efficiency for an assembly of particles in a rotating drum or any other crushing device.

Fig. 7 shows particle damage D_w as a function of the impact velocity v for several values of the fracture energy G_f. The data follow an S-shaped curve in which the damage first increases rapidly with v and then slowly tends to 1. As expected, particle damage for a given value of v declines as G_f increases. The asymptotic value $D_w = 1$ corresponds to the limit case where the particle fully breaks into its building cells. We also see that the error bars are small, indicating that the variability of fracture as a result of the variations of impact position is not an influential factor.

Fig. 8 shows the fragmentation efficiency η as a function of v for different values of G_f. We see that η is unmonotonic: it increases rapidly with v up to a value of the order of 0.3 and then slowly declines towards zero. The velocity at which η takes its peak value increases with G_f. Such an optimum value for energy utilization as a function of the supplied energy per unit mass was

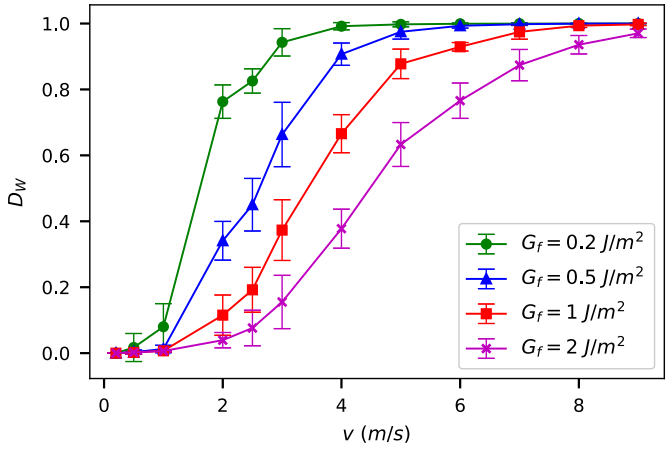

Fig. 7. Particle damage D_w as a function of impact velocity v for different values of fracture energy G_f and $C_n = C_t = 1$ MPa. For each test, the error bar represents standard deviation over 10 independent tests.

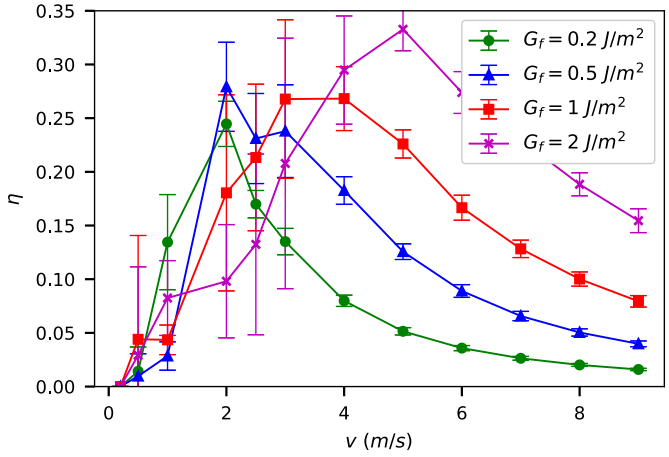

Fig. 8. Fragmentation efficiency η as a function of impact velocity v for several values of fracture energy, C_n and C_t were kept constant at 1 MPa.

also observed in impact experiments of quartz beads of different sizes (Rumpf, 1973). This unmonotonic behavior means that there is a characteristic velocity at which the conversion of kinetic energy to fracture energy is optimal. Below and above the characteristic velocity the supplied energy is mostly either dissipated by inelastic collisions or taken away by the fragments. The energy consumed by fragment motions and inelastic collisions at the characteristic velocity is almost two times larger than the fracture energy.

Since the different plots of D_w and η differ according to the value of the fracture energy G_f, we expect that they can be collapsed on the same plot when considered as a function of the supplied energy W_k^- (rather than the impact velocity) normalized by $W_f^T = s^T G_f$. Up to statistical fluctuations, this is indeed what we observe in Figs. 9 and 10, displaying D_w and η as a function of the normalized impact energy defined by

$$\omega = \frac{W_k^-}{W_f^T}. \tag{15}$$

The fitting form shown in Fig. 10 is given by

$$\eta(\omega) = \frac{a\omega/\omega^*}{1 + (\omega/\omega^*)^2}, \tag{16}$$

with $a = 0.55$ and $\omega^* = 1.81$. In this approximation of the collapsed data, the peak value of η is $\simeq 0.27$ and it occurs for $\omega = \omega^*$. This value means that the amount of impact energy required to fracture the particle into its building blocks (cells) is almost two

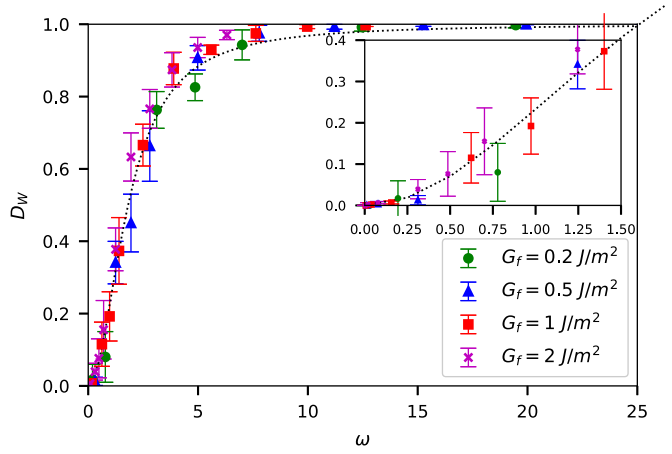

Fig. 9. Particle damage D_w as a function of the normalized impact energy ω. The dotted line is the fitting form (21). The error bars represent standard deviation for 10 independent events. The inset shows the same plot in the range $\omega < 1.5$ together with a quadratic fit.

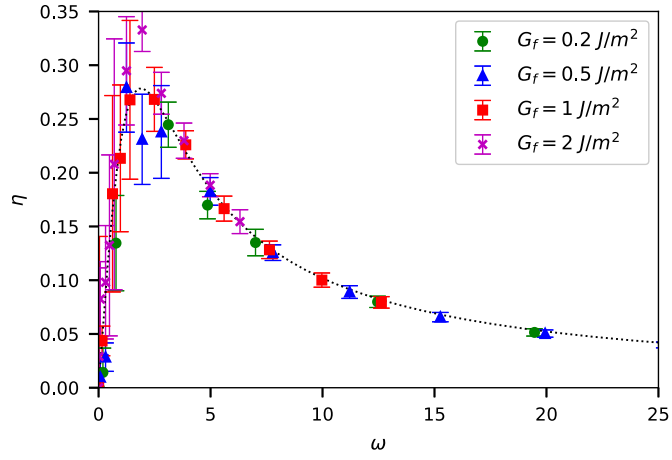

Fig. 10. Fragmentation efficiency η as a function of the normalized impact energy ω. The dotted line is the fitting form (20). The error bars represent standard deviation for 10 independent events.

times the total fracture energy of the particle, and the fragmentation efficiency is only 27% for this amount of the supplied energy.

The fitting form (16) can be understood by first noting that Eqs. (13)–(15) yield the relation

$$\eta = \frac{D_w}{\omega}. \tag{17}$$

At low values of ω i.e. ($\omega < 1.8$), the data points in Fig. 9 suggest that D_w in this regime increases quadratically with ω; see the inset to Fig. 9. Hence, according to (17), η increases linearly with ω. On the other hand, at large values of ω, D_w tends to 1 so that η asymptotically declines as $1/\omega$. The fitting form (16) is the simplest interpolation between these two asymptotic behaviors. Eqs. (16) and (17), yield the following fitting form for D_w as a function of ω:

$$D_w(\omega) = \omega\eta = a\omega^* \frac{(\omega/\omega^*)^2}{1 + (\omega/\omega^*)^2}, \tag{18}$$

Since D_w tends by definition to 1 as $\omega \to \infty$, we have

$$a = \frac{1}{\omega^*}. \tag{19}$$

This relation is consistent with our numerical data and it reduces the number of parameters in Eq. (16) to a single parameter, so that we have

$$\eta(\omega) = \frac{1}{\omega^*} \frac{\omega/\omega^*}{1 + (\omega/\omega^*)^2}, \tag{20}$$

$$D_w(\omega) = \frac{(\omega/\omega^*)^2}{1 + (\omega/\omega^*)^2}. \tag{21}$$

Both functions are in good agreement with the data shown in Figs. 9 and 10.

4. Restitution coefficient

We now consider two more dimensionless variables that characterize the transfer of kinetic energy from the impacting particle to the fragments. We define an effective restitution coefficient e_k from the ratio of the pre-impact and post-impact kinetic energies:

$$e_k^2 = \frac{W_k^+}{W_k^-}. \tag{22}$$

This coefficient can take a nonzero value even when the restitution coefficient e between the particle and the impacted plane or between the fragments is zero. Another variable of interest is the ratio of the post-impact kinetic energy to the fracture energy:

$$\chi = \frac{W_k^+}{W_f}. \tag{23}$$

This variable simply reflects the relative importance of the energy transported by the fragments with respect to that consumed in particle fragmentation.

Fig. 12 shows χ as a function of ω on the log-log and linear scales. We see that χ is nearly constant and quite small ($\simeq 0.3$) in the range $\omega < \omega^* \simeq 1.8$ and then increases approximately as a power-law function:

$$\chi(\omega) = c\left(\frac{\omega}{\omega^*}\right)^{\alpha} \quad \text{for } \omega > \omega^*, \tag{24}$$

with $\alpha \simeq 1.12$ and c slightly increasing with G_f. For G_f varying from $0.2\,\mathrm{J/m^2}$ to $2\,\mathrm{J/m^2}$, c varies from 0.3 to 0.5, as observed in inset to Fig. 12. The kinetic energy of the fragments being negligibly small as compared to the energy consumed for fracture in the low-energy regime, all the supplied kinetic energy is either used for fracture or dissipated by inelastic collisions and friction. The amount of dissipation by collisions and friction is given by

$$W_c = W_k^- - W_k^+ - W_f \equiv \left(\frac{1}{\eta} - \chi - 1\right) W_f. \tag{25}$$

It has its lowest value $W_c/W_f \simeq 2.2$ at ω^* where $\eta \simeq 0.27$.

Fig. 11 shows e_k^2 as a function of ω. It is nearly constant and small in the low-energy regime ($\omega < \omega^*$) and then grows with ω. It is easy to see that

$$e_k^2 = \chi\eta \tag{26}$$

In the low-energy regime, we have $e_k \simeq 0$ as χ is negligible. At higher energies, we have

$$e_k^2 = \chi\eta = \frac{c}{\omega^*} \frac{(\omega/\omega^*)^{\alpha+1}}{1 + (\omega/\omega^*)^2}. \quad \text{for } \omega > \omega^* \tag{27}$$

This form fits well the data as shown in Fig. 11. We see that as $\omega \to \infty$, e_k^2 varies asymptotically as $\omega^{1/2}$.

5. Influence of stress thresholds on the fracture process

In the last section, we extensively analyzed the effect of impact energy and fracture energy on the particle fragmentation for a constant value of the stress thresholds C_n and C_t as well as the

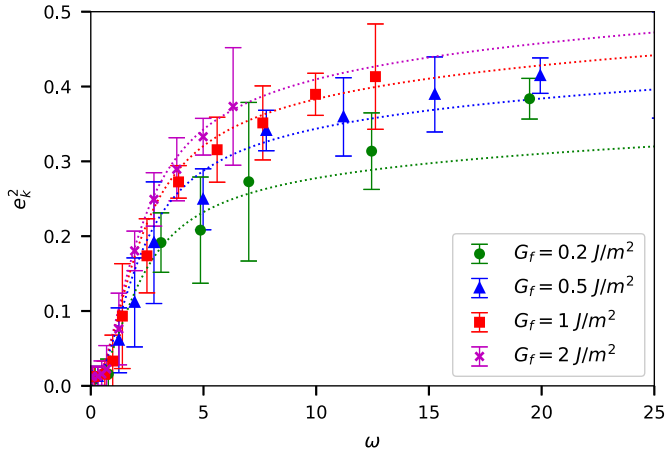

Fig. 11. Squared restitution coefficient e_k^2 as a function of ω. The dotted lines represent the fitting form (27) with the corresponding values of c (see inset to Fig. 12). The error bars represent standard deviation for 10 independent events.

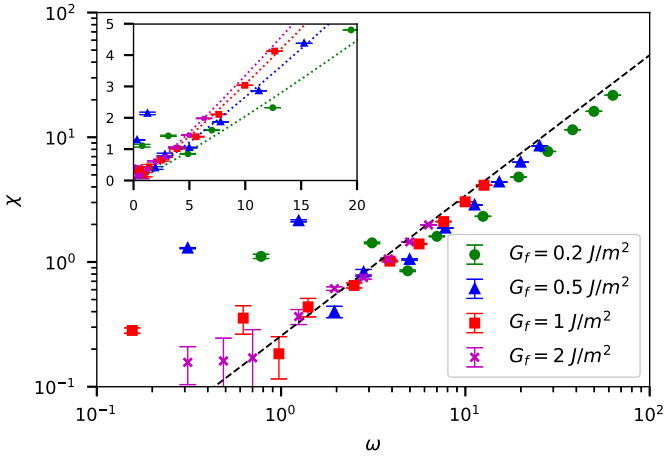

Fig. 12. Variable χ as a function of ω. The dashed line represents a power-law function $\propto\omega^{\alpha}$ with $\alpha \simeq 1.12$. The inset shows the same data on the linear scale. The dotted lines are different fits with the same value of α but different values of the prefactor c; see Eq. (24). The error bars represent standard deviation for 10 independent events.

friction coefficient between fragments. In this section, we consider the effect of stress thresholds.

Fig. 13 shows particle damage D_w as a function of C_n for three values of the impact velocity v. As expected for small values of C_n, the particle is fully damaged (D_w=1) but as C_n increases, D_w declines and tends to a constant value close to 0. For a given value of C_n, particle damage is higher for larger velocity. Actually, the values of C_n can be compared to the mean stress generated during the collision of the particle with the plane. The mean stress is given by the momentum exchange mv, where m is particle mass, divided by collision duration, which is equal to the time step δt in our CD simulations, and by the total cell-cell interface s^T. The same data are shown in the inset of Fig. 13 as a function of the normalized stress $C_n s^T \delta t/(mv)$. We see that within statistical fluctuations the data for the three values of v collapse on the same curve. It is important to remark here that the collision duration is an important parameter for this scaling. For a compliant particle, the collision duration depends on the elastic moduli of the particle and $mv/\delta t$ should be replaced by the largest force achieved during collision.

Another parameter that may influence particle fracture is the ratio $\psi = C_t/C_n$. Fig. 14 shows D_w as a function of ω for different values of ψ. Within statistical fluctuations, all the data coin-

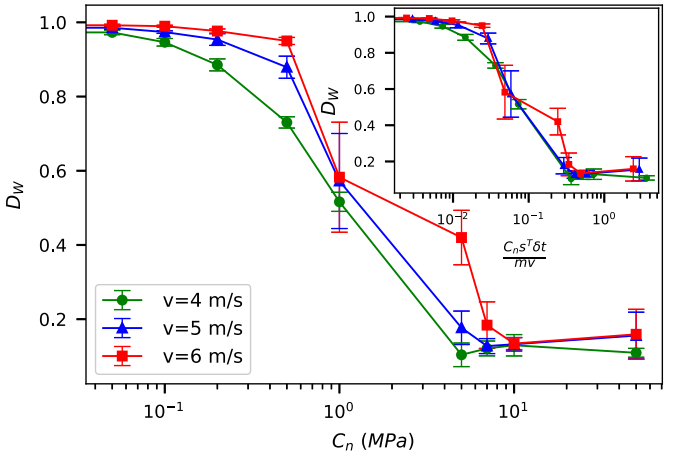

Fig. 13. Particle damage D_w as a function of the normal stress threshold C_n for three values of impact velocity v for $G_f = 1$ J/m^2. The inset shows the same data for the values of C_n normalized by the impulsion $mv/(s^T\delta t)$, where mv is the change of momentum during collision and δt is collision time. The error bars represent standard deviation for 10 independent events.

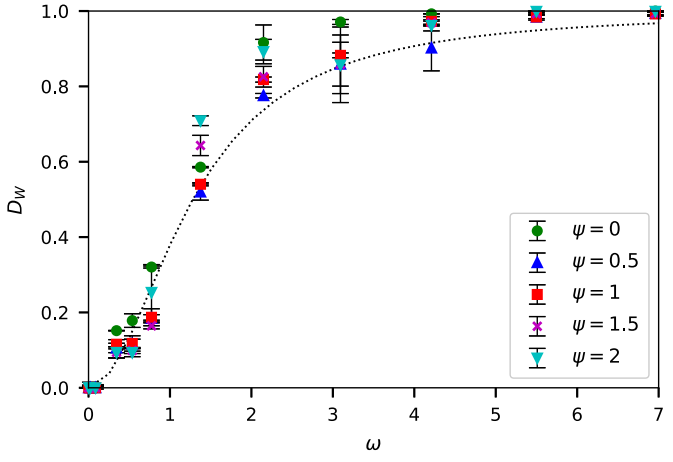

Fig. 14. Particle damage D_w as a function of ω for different values of $\psi = C_t/C_n$. The dotted line is the fitting form (21). The error bars represent standard deviation for 10 independent events.

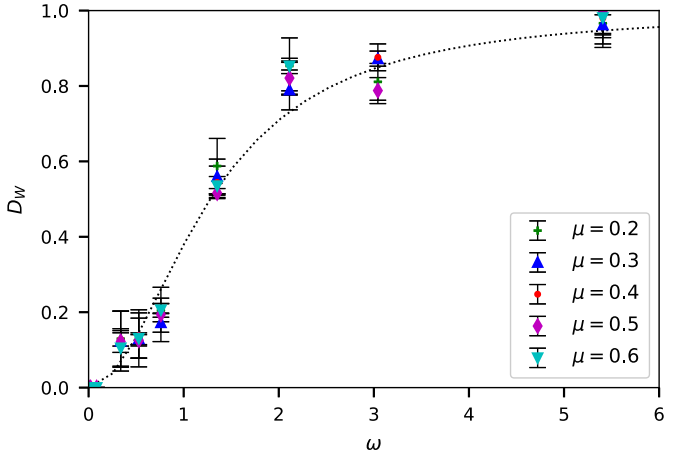

Fig. 15. Particle damage D_w as a function of friction coefficient μ between cohesionless cells. The dotted line is the fitting form (21). The error bars represent standard deviation for 10 independent events.

cide. Interestingly, even for $C_t = 0$, we observe the same behavior, meaning that the fracture basically occurs in tensile mode. Relative tangential displacements between cells are obviously incompatible with the kinematic constraints. But this does not exclude the activation of the shear mode in the case of an oblique collision between the particle and the impacted surface. We also observe that the friction coefficient μ, activated only at cell-cell interfaces having lost their cohesion, has no influence on the fracture as shown in Fig. 15.

6. Conclusions and perspectives

In this paper, we used 3D DEM numerical simulations to analyze the fragmentation of a single particle impacting a rigid plane. The particle is discretized by means of Voronoï tessellation into polyhedral cells representing potential fragments. The cell-cell interfaces are governed by a fracture law combining material strength and fracture energy as necessary and sufficient criteria for debonding. In this model, the ratio of the fracture energy to material strength corresponds to the minimum inelastic deformation before particle fracture.

We showed that particle damage, i.e. the proportion of fractured interfaces, and the amount of energy consumed for fragmentation scale with the initial kinetic energy of the impacting particle normalized by fracture energy. The fragmentation efficiency, defined as fragmentation energy normalized by the impact energy, is unmonotonic as a function of impact energy with optimal efficiency occurring for a well defined value of the impact velocity. We introduced a functional form that fits the collapsed data with a single free parameter. Similar fitting forms were proposed for the damage and effective restitution coefficient. We also showed that particle damage scales with the normal stress threshold normalized by the mean impact stress.

All the results presented in this numerical investigation show consistently the ability of our numerical approach to handle dynamic fragmentation of single particles. It can be applied to simulate the compaction and shear of an assembly of crushable particles in which the behavior of a single particle can provide insights into the collective evolution of particles and their fragments. The most basic limitation of this approach, as in all DEM simulations, is the number of potential fragments that can be produced in the comminution process. Nevertheless, it is a powerful tool for a detailed analysis of the local events and re-distribution of energy inside the granular material. For example, in this paper we found that the fragmentation efficiency is at most 30% in the single particle impact tests. The query here is whether such a level of efficiency can be reached in a collective fragmentation process of particles.

Finally, in the case of a single particle, we did not analyze in this paper the crack growth, fragment shapes and sizes for different levels of fracture energy, and fracture modes of the particle. These features will be presented elsewhere.

References

Bailon-Poujol, I., Bailon, J.P., L'Espérance, G., 2011. Ball-mill grinding kinetics of master alloys for steel powder metallurgy applications. Powder Technol. 210 (3), 267–272. doi:10.1016/j.powtec.2011.03.028.

Bruchmüller, J., van Wachem, B., Gu, S., Luo, K., 2011. Modelling discrete fragmentation of brittle particles. Powder Technol. 208 (3), 731–739. https://doi.org/10.1016/j.powtec.2011.01.017.

Brzesowsky, R., Spiers, C., Peach, C., Hangx, S., 2011. Failure behavior of single sand grains: theory versus experiment. J. Geophys. Res. Solid Earth 116 (B6), B06205/1–B06205/13.

Cantor, D., Azéma, E., Sornay, P., Radjai, F., 2017. Three-dimensional bonded-cell model for grain fragmentation. Computational Particle Mechanics 4 (4), 441–450. doi:10.1007/s40571-016-0129-0.

Casini, F., Viggiani, G.M., Springman, S.M., 2013. Breakage of an artificial crushable material under loading. Granul. Matter 15 (5), 661–673.

Chau, K.T., Wei, X.X., Wong, R.H.C., Yu, T.X., 2000. Fragmentation of brittle spheres under static and dynamic compressions: experiments and analyses. Mech. Mater. 32 (9), 543–554. doi:10.1016/S0167-6636(00)00026-0.

Ciantia, M., de Toledo, M.A.A., Calvetti, F., Solé, A.G., 2015. An approach to enhance efficiency of DEM modelling of soils with crushable grains. Géotechnique 65 (2), 91–110.

Cundall, P.A., 1988. Formulation of a three-dimensional distinct element model–Part I. A scheme to detect and represent contacts in a system composed of many polyhedral blocks. Int. J. Rock Mech. Min. Sci. 25 (3), 107–116. doi:10.1016/0148-9062(88)92293-0.

Cundall, P.A., Strack, O.D.L., 1979. A discrete numerical model for granular assemblies. Géotechnique 29 (1), 47–65.

Delenne, J.-Y., Youssoufi, M.S.E., Cherblanc, F., Bénet, J.C., 2004. Mechanical behaviour and failure of cohesive granular materials granular materials. Int. J. Numer. Anal. Methods Geomech. 28 (15), 1577–1594.

Dubois, F., Jean, M., Renouf, M., Mozul, R., Martin, A., Bagneris, M., 2011. LMGC90. In: Proceedings of the 10e colloque national en calcul des structures.

Eliáš, J., 2014. Simulation of railway ballast using crushable polyhedral particles. Powder Technol. 264, 458–465. doi:10.1016/j.powtec.2014.05.052.

Fuerstenau, D.W., Abouzeid, A.Z., 2002. The energy efficiency of ball milling in comminution. Int. J. Miner. Process. 67 (1–4), 161–185. doi:10.1016/S0301-7516(02)00039-X.

Galindo-Torres, S., Pedroso, D., Williams, D., Li, L., 2012. Breaking processes in three--dimensional bonded granular materials with general shapes. Comput. Phys. Commun. 183 (2), 266–277.

Ge, R., Ghadiri, M., Bonakdar, T., Hapgood, K., 2017. 3D printed agglomerates for granule breakage tests. Powder Technol. 306, 103–112. doi:10.1016/j.powtec.2016.10.070.

Giacomini, A., Buzzi, O., Renard, B., Giani, G.P., 2009. Experimental studies on fragmentation of rock falls on impact with rock surfaces. Int. J. Rock Mech. Min. Sci. 46 (4), 708–715. doi:10.1016/j.ijrmms.2008.09.007.

Govender, I., 2016. Granular flows in rotating drums: a rheological perspective. Miner. Eng. 92, 168–175. doi:10.1016/j.mineng.2016.03.021.

Herrmann, H.J., Luding, S., 1998. Modeling granular media with the computer. Contin. Mech. Thermodyn. 10, 189–231.

Hillerborg, A., Modéer, M., Petersson, P.E., 1976. Analysis of crack formation and crack growth in concrete by means of fracture mechanics and finite elements. Cem. Concr. Res. 6, 773–782.

Huang, J., Xu, S., Hu, S., 2014. Influence of particle breakage on the dynamic compression responses of brittle granular materials. Mech. Mater. 68, 15–28.

Jean, M., Acary, V., Monerie, Y., 2001. Non-smooth contact dynamics approach of cohesive materials. Philos. Trans. R. Soc. Lond. A: Math. Phys. Eng. Sci. 359 (1789), 2497–2518.

Kim, S., Santamarina, J.C., 2016. Rock Crushing Using Microwave Pre-treatment. In: Proceedings of the Geo-Chicago. August, pp. 720–729. doi:10.1061/9780784480151.071.

Kun, F., Herrmann, H., 1998. Transition from damage to fragmentation in collision of solids. Phys. Rev. E 59 (3), 2623–2632. doi:10.1103/PhysRevE.59.2623. 9810315.

Kun, F., Herrmann, H.J., 1996. A study of fragmentation processes using a discrete element method. Comput. Methods Appl. Mech. Eng. 138, 3–18.

Laubie, H., Radjai, F., Pellenq, R., Ulm, F.J., 2017. Stress transmission and failure in disordered porous media. Phys. Rev. Lett. 119, 075501.

Leguillon, D., 2002. Strength or toughness? A criterion for crack onset at a notch. Eur. J. Mech. A/Solids 21, 61–72.

Leite, F.d.C.a., dos Santos Motta, R., Vasconcelos, K.L., Bernucci, L., 2011. Laboratory evaluation of recycled construction and demolition waste for pavements. Constr. Build. Mater. 25 (6), 2972–2979. doi:10.1016/j.conbuildmat.2010.11.105.

Lobo-Guerrero, S., Vallejo, L.E., Vesga, L.F., 2006. Visualization of crushing evolution in granular materials under compression using DEM. Int. J. Geomech. 6 (3), 195–200. doi:10.1061/(ASCE)1532-3641(2006)6:3(195).

Luding, S., 2008. Cohesive, frictional powders: contact models for tension. Granul. Matter 10 (4), 235–246. doi:10.1007/s10035-008-0099-x.

Mayer-Laigle, C., Blanc, N., Rajaonarivony, R.K., Rouau, X., 2018. Comminution of dry lignocellulosic biomass, a review: part I. From fundamental mechanisms to milling behaviour. Bioengineering 5 (2). doi:10.3390/bioengineering5020041.

McDowell, G., Harireche, O., 2002. Discrete element modelling of soil particle fracture. Géotechnique 52 (2), 131–135.

Mishra, B.K., Thornton, C., 2001. Impact breakage of particle agglomerates. Int. J. Miner. Process. 61 (4), 225–239. doi:10.1016/S0301-7516(00)00065-X.

Moreau, J., Solids, A., 1994. Some numerical methods in multibody dynamics: application to granular. Eur. J. Mech. 13, 93–114.

Moreau, J.J., 1993. New Computation Methods in Granular Dynamics. In: Proceedings of the Powders & Grains, 93. A. A. Balkema, Rotterdam, p. 227.

Moreno-Atanasio, R., Ghadiri, M., 2006. Mechanistic analysis and computer simulation of impact breakage of agglomerates: effect of surface energy. Chem. Eng. Sci. 61 (8), 2476–2481. doi:10.1016/j.ces.2005.11.019.

Nguyen, D.-H., Azéma, E., Sornay, P., Radjai, F., 2015. Bonded-cell model for particle fracture. Phys. Rev. E 91, 022203. doi:10.1103/PhysRevE.91.022203.

Potapov, A.V., Campbell, C.S., 1994. Computer simulation of impact-induced particle breakage. Powder Technol. 81, 207–216. doi:10.1016/0032-5910(94)02907-5.

Quey, R., Dawson, P.R., Barbe, F., 2011. Large-scale 3D random polycrystals for the finite element method: generation, meshing and remeshing. Comput. Methods Appl. Mech. Eng. 200 (17–20), 1729–1745. doi:10.1016/j.cma.2011.01.002.

Radjai, F., Richefeu, V., 2009. Contact dynamics as a nonsmooth discrete element method. Mech. Mater. 41 (6), 715–728.

Rice, J., 1978. Thermodynamics of the quasi-static growth of griffith cracks. J. Mech. Phys. Solids 26, 61–78.

Rumpf, H., 1973. Physical aspects of comminution and new formulation of a law of comminution. Powder Technol. 7 (3), 145–159. doi:10.1016/0032-5910(73)80021-X.
Salman, A.D., Biggs, C.A., Fu, J., Angyal, I., Szabó, M., Hounslow, M.J., 2002. An experimental investigation of particle fragmentation using single particle impact studies. Powder Technol. 128 (1), 36–46. doi:10.1016/S0032-5910(02)00151-1.
Stamboliadis, E.T., 2007. The energy distribution theory of comminution specific surface energy, mill efficiency and distribution mode. Miner. Eng. 20 (2), 140–145. doi:10.1016/j.mineng.2006.07.009.
Subero, J., Ning, Z., Ghadiri, M., Thornton, C., 1999. Effect of interface energy on the impact strength of agglomerates. Powder Technol. 105 (1–3), 66–73. doi:10.1016/S0032-5910(99)00119-9.
Taboada, A., Estrada, N., Radjai, F., 2006. Additive decomposition of shear strength in cohesive granular media from grain-scale interactions. Phys. Rev. Lett. 97 (9), 098302.
Tarasiewicz, S., Radziszewski, P., 1990. Comminution energetics part I: breakage energy model. Mater. Chem. Phys. 25 (1), 1–11. doi:10.1016/0254-0584(90)90002-R.
Tavares, L., King, R., 1998. Single-particle fracture under impact loading. Int. J. Miner. Process. 54 (July), 1–28. doi:10.1016/S0301-7516(98)00005-2.
Thornton, C., Yin, K.K., Adams, M.J., 1996. Numerical simulation of the impact fracture and fragmentation of agglomerates. J. Phys. D: Appl. Phys. 29, 424–435.
Timár, G., Blömer, J., Kun, F., Herrmann, H.J., 2010. New universality class for the fragmentation of plastic materials. Phys. Rev. Lett. 104 (9), 1–4. doi:10.1103/PhysRevLett.104.095502. 1002.2807.
Touil, D., Belaadi, S., Frances, C., 2006. Energy efficiency of cement finish grinding in a dry batch ball mill. Cem. Concr. Res. 36 (3), 416–421. doi:10.1016/j.cemconres.2005.12.005.
Tsoungui, O., Vallet, D., Charmet, J., 1999. Numerical model of crushing of grains inside two-dimensional granular materials. Powder Technol. 105, 190–198.
Varnes, D.J., 1958. Landslide types and processes. Landslides Eng. Pract. 29 (3), 20–45.
Vogel, L., Peukert, W., 2003. Breakage behaviour of different materials - construction of a mastercurve for the breakage probability. Powder Technol. 129 (1–3), 101–110. doi:10.1016/S0032-5910(02)00217-6.
Wittel, F.K., Carmona, H.A., Kun, F., Herrmann, H.J., 2008. Mechanisms in impact fragmentation. Int. J. Fract. 154 (1–2), 105–117. doi:10.1007/s10704-008-9267-6.
Wu, S.Z., Chau, K.T., Yu, T.X., 2004. Crushing and fragmentation of brittle spheres under double impact test. Powder Technol. 143–144, 41–55. doi:10.1016/j.powtec.2004.04.028.
Xu, M., Hong, J., Song, E., 2017. DEM study on the effect of particle breakage on the macro and micro-behavior of rockfill sheared along different stress paths. Comput. Geotech. 89, 113–127. (Supplement C). doi: 10.1016/j.compgeo.2017.04.012.
Zubelewicz, A., Bažant, Z.P., 1987. Interface element modeling of fracture in aggregate composites. J. Eng. Mech. 113 (11), 1619–1630.